HST proper motions on the far side of the Galactic bar-data

Soto, M.; Kuijken, K.H.; Rich, R.M.; Clarkson, W.I.; Nilo Castellón, J.L.; Fernández-Trincado, J.G.; ... ; Vieira, K.

Monthly Notices of the ROYAL ASTRONOMICAL SOCIETY

MNRAS **524,** 224–234 (2023) https://doi.org/10.1093/mnras/stad1911
Advance Access publication 2023 June 26

HST proper motions on the far side of the Galactic bar—data

Mario Soto [1]★ Konrad Kuijken,[2]★ R. Michael Rich [3] William I. Clarkson,[4] José Luis Nilo Castellón,[5] José G. Fernández-Trincado,[6] Rodrigo Contreras Ramos,[7,8] Andrea Kunder,[9] Laura D. Baravalle,[10,11] M. Victoria Alonso,[10,11] Iulia T. Simion,[12] Christian I. Johnson[13] and Katherine Vieira[1]

[1]*Instituto de Astronomía y Ciencias Planetarias, Universidad de Atacama, Av. Copayapu 485, Copiapó, Chile*
[2]*Leiden Observatory, Leiden University, PO Box 9513, NL-2300 RA Leiden, The Netherlands*
[3]*Department of Physics and Astronomy, UCLA, 430 Portola Plaza, Box 951547, Los Angeles, CA 90095-1547, USA*
[4]*Department of Natural Sciences, University of Michigan-Dearborn, 4901 Evergreen Road, Dearborn, MI 48128, USA*
[5]*Departamento de Astronomía, Universidad de La Serena, Av. Juan Cisternas 1200, La Serena, Chile*
[6]*Instituto de Astronomía, Universidad Católica del Norte, Av. Angamos 0610, Antofagasta, Chile*
[7]*Millennium Institute of Astrophysics, Av. Vicuña Mackenna 4860, 782-0436 Macul, Santiago, Chile*
[8]*Departamento de Astronomía y Astrofísica, Pontificia Universidad Católica de Chile, Vicuña Mackena 4860, Casilla 306, Santiago 22, Chile*
[9]*Saint Martin's University, 5000 Abbey Way SE, Lacey, WA 98503 USA*
[10]*Observatorio Astronómico de Córdoba, Universidad Nacional de Córdoba, Laprida 854, X5000BGR Córdoba, Argentina*
[11]*Instituto de Astronomía Teórica y Experimental (IATE, CONICET-UNC), Laprida 854, Córdoba, X5000BGR, Argentina*
[12]*Key Laboratory for Research in Galaxies and Cosmology, Shanghai Astronomical Observatory, 80 Nandan Road, Shanghai 200030, China*
[13]*Space Telescope Science Institute, 3700 San Martin Drive, Baltimore, MD 21218, USA*

Accepted 2023 June 15. Received 2023 June 11; in original form 2022 October 27

ABSTRACT

This is the third paper in a series that attempts to observe a clear signature of the Galactic bar/bulge using kinematic observations of the bulge stellar populations in low foreground extinction windows. We report on the detection of ∼100 000 new proper motions in four fields covering the far side of the Galactic bar/bulge, at negative longitudes. Our proper motions have been obtained using observations from the Advance Camera for Surveys (ACS), on board of the *Hubble Space Telescope* (*HST*), with a time-baseline of 8–9 years, which has produced accuracies better than 0.5 mas yr^{-1} for a significant fraction of the stellar populations with $F814W < 23$ mag. Interestingly, as shown in previous works, the Hess diagrams show a strikingly similar proper motion distribution to fields closer to the Galactic center and consistent with an old stellar population. The observed kinematics point to a significant bulge rotation, which seems to predominate even in fields as far as $l \simeq -8°$, and is also reflected in the changes of the velocity ellipsoid in the l, b plane as a function of distance.

Key words: methods: data analysis – Galaxy: bulge – Galaxy: kinematics and dynamics – Galaxy: stellar content.

1 INTRODUCTION

The Galactic bulge still surprises us with its features and complexity (Recio-Blanco et al. 2017; Rojas-Arriagada et al. 2020; Fernández-Trincado et al. 2020). Since de Vaucouleurs (1964) proposed that our Galactic bulge is actually a bar, we have advanced considerably in our understanding of the structure of the Milky Way (e.g. Blitz & Spergel 1991; Weiland et al. 1994; Nataf et al. 2010; Wegg & Gerhard 2013) as well as the composition (e.g. McWilliam & Rich 1994; Johnson et al. 2014; Zoccali et al. 2017) and ages (e.g. Ortolani et al. 1995; Valenti et al. 2013; Hasselquist et al. 2020; Savino et al. 2020) of the stellar populations that make up the inner Galaxy. Evidence from the *Cosmic Background Explorer* (COBE; Dwek et al. 1995) showed that the best fit for its observations of the Galactic bulge, based on 2.2 μm observations, was a boxy bulge that could be deprojected in a triaxial distribution with an inclination angle of between 10° and 30°. Since then, both the inclination angle and the exact triaxial distribution have been the subject of much analysis (e.g. Robin et al. 2012; Wegg & Gerhard 2013).

Despite more than 60 yr of intense observational study, the bulge remains a challenging observational target. Indeed, many of its first-order parameters (such as the bar angle) remain controversial. For example, Vanhollebeke, Groenewegen & Girardi (2009) and, more recently Simion et al. (2017) provide compilations of bar parameters in the pre-*Gaia* literature, showing no convergence over time: the derived parameters of the bar appear to depend on the population selected to measure it. In particular, Simion et al. (2017) find a strong degeneracy between the viewing angle of the bar and the dispersion of the Red Clump (RC) absolute magnitude distribution when using near-IR (NIR) data from the VISTA Variables in the Vía Láctea survey (Minniti et al. 2010).

The spatial distribution and motions of stars in the bulge depend on their location within the bulge (e.g. their Galactic latitude, longitude, and galactocentric distance, see e.g. Ness et al. 2013; Queiroz et al. 2021; Simion et al. 2021) and may also correlate with metallicity (e.g. Babusiaux et al. 2010; Zoccali & Valenti 2016; Zoccali et al. 2017; Clarkson et al. 2018; Lian et al. 2021; Queiroz et al. 2021, and references therein) and age (e.g. Catchpole

★ E-mail: mario.soto@uda.cl (MS); kuijken@strw.leidenuniv.nl (KK)

et al. 2016). The kinematics of the bulge stars can be explained by a composite population experiencing bar-buckling (e.g. Shen et al. 2010; Debattista et al. 2017, 2019), and it is the complicated joint distribution of positions, velocities, and chemical abundances (metallicity and α-enhancement; Zasowski et al. 2019) that form the body of evidence against which our understanding of the formation and evolution of the bulge must now be tested.

The advent of *Gaia* (Gaia Collaboration et al. 2016), currently in its third data release (DR3; Gaia Collaboration et al. 2023), has revolutionized the understanding of the Milky Way structure and content by allowing the analysis of the stellar populations not only in terms of photometry or spectroscopy data sets, but also including parallax distances and proper motions for a significant number of stars of the Galactic disk. Furthermore, these advances have also clearly impacted the understanding of the kinematics of globular clusters and dwarf galaxies around the Milky Way (Gaia Collaboration et al. 2018b). However, the bulge is a challenging target for *Gaia* due to the high degree of spatial crowding and the strong, variable extinction: most stars at or below the main sequence turn-off are both too crowded and too faint for *Gaia* to measure precise proper motions (e.g. Gaia Collaboration et al. 2018a). Thus, many of the recent studies based on *Gaia* data regarding bulge kinematics have been limited to the red giant branch (RGB) or RC populations (Queiroz et al. 2021; Simion et al. 2021).

For precision proper motions in the bulge, *HST*, and now the *JWST*, are the facilities of choice. With *HST*, precision photometry and relative astrometry for populations well below the bulge main sequence turn-off can be obtained (provided the extinction is not too great). This carries several advantages: first, accurate photometry of faint diagnostic features in the colour-magnitude diagram (CMD), like the main sequence or turn-off, allows direct diagnostics for the metallicity and age distribution (e.g. Brown et al. 2010; Gennaro et al. 2015). Second, by probing the much more populous main sequence objects, the majority population is directly sampled, providing an important check on the rarer evolved objects (e.g. Cohen et al. 2010) and allowing dissection by distance along the line of sight, complementing fan-beam spectroscopic surveys (e.g. Clarkson et al. 2018, and references therein). Third, *HST* (and currently *only HST* and JWST) can be used to measure relative proper motions for large samples (typically $\sim 10^{4-5}$ stars in a single $\sim 3'$ field of view) of main sequence stars, directly measuring the kinematics of the underlying stellar population and measuring bulge rotation.

This approach was pioneered by Kuijken & Rich (2002), who started this sub-field by demonstrating the separation of bulge and disk populations via tagging by relative proper motion. Kuijken & Rich (2002) used WFPC2 proper motions to measure the rotation of the bulge in two low-reddening windows. Building from this early result, we have pursued a long-term campaign to measure the main parameters of the bar, including the extent of the bar and its pattern speed, using *HST*to measure proper motions over a range of locations within the inner $20^\circ \times 20^\circ$ of the Milky Way, supplemented with radial velocities where available. An early result from this campaign was an initial estimate of the vertical gravitational acceleration along the minor axis of the Galaxy from the three minor-axis fields (Kuijken 2004). Additional results from the first six fields in this campaign, including detections of vertex deviation in six bulge fields along the bulge minor axis (Soto, Kuijken & Rich 2012; hereafter Paper I) and at positive longitudes (Soto et al. 2014; hereafter Paper II), have been previously presented.

Here, we communicate techniques and results from four fields on the *far* side of the bar. Our fields are chosen to sample kinematic features of the orbits on this region, which should help to constrain important Galactic structural parameters such as the bar spatial extent and pattern speed.

The effects of extinction towards the Galactic bulge have customarily been mitigated using two strategies: minimize extinction by using observations in wavelengths less affected by reddening, such as near infrared, or focus the observations in regions of the bulge where we know the extinction is limited, customarily called 'windows'. While the former is the case of NIR surveys such as the Two Micron All Sky Survey (2MASS; Skrutskie et al. 2006), the Deep Infrared Survey of the Southern Sky (DENIS; Epchtein et al. 1994), or the more recent VVV survey and its continuation VVV*X*, the latter has been limited to a few regions such as Baade's Window (e.g. Spaenhauer, Jones & Whitford 1992; Zhao, Spergel & Rich 1994; Soto, Rich & Kuijken 2007), Sagittarius-I (e.g. Clarkson et al. 2008; henceforth Cl08), and Plaut's window (e.g. Vieira et al. 2007), to name a few.

This paper reports the observations and analysis of the four fields on the far side of the bar, the description of the rich kinematic data set thus produced, and a few preliminary results from the inter-comparison of this set of four fields. The use of the complete ensemble of proper motions between all ten fields of our campaign is not a trivial task, and is deferred to future communications.

This paper is organized as follows: in Section 2 we describe the HST ACS/WFC observations used to calculate the stellar motions, while Section 3 presents the proper motion procedure itself, including the astrometric and photometric corrections applied. The analysis of our results and their implication in our conception of the Galactic structure are laid out in Section 4. Finally, our findings are summarized in Section 5.

2 OBSERVATIONS

The four fields chosen to complete the observational campaign constitute two pairs of samples roughly parallel to the Galactic mid-plane. One pair of fields at $b \approx -7^\circ$ extends the positive-latitude off-axis sample of Soto et al. (2014) to the far side of the bar. The other pair samples similar longitudes to the first, but at $b \approx +4^\circ$ probes slightly closer to the opposite side of the Galactic mid-plane. Therefore, the four new fields allow pair-wise comparison of kinematic trends between fields, ultimately allowing comparisons across the entire bulge. Fig. 1 places the four fields in context of the wider observational campaign, which now consists of three fields along the minor axis (white circles in Fig. 1), three at longitude $b \approx -8^\circ$ along positive longitudes (grey circles in Fig. 1), and the four fields at negative longitudes (grey squares in Fig. 1). One of the main scientific considerations in the selection of the fields of this project is that the extinction towards the field must allow precision kinematics to a sufficient depth that the main sequence populations of interest are well-sampled. Table 1 and Fig. 1 summarize the observations corresponding to the four fields on the far side of the Galactic bar, at negative Galactic longitudes, in this work; Field-4 + 5 [$(l, b) = (356.^\circ00, 4.^\circ95)$], Field-8 + 5 [$(l, b) = (352.^\circ00, 4.^\circ53)$], Field-4-7 [$(l, b) = (356.^\circ02, -7.^\circ04)$], and Field-8-7 [$(l, b) = (352.^\circ50, -7.^\circ00)$]. Observations of all our fields were taken with ACS onboard the HST during 2003 (GO-9816; P.I.: Kuijken) and 2010 (GO-11655; P.I.: Kuijken) for the first and second epoch, respectively. The F814W filter was chosen for our astrometric observations since it has a relatively well-sampled point spread function (PSF), and the distortion solution in this filter is very well-constrained (e.g. Anderson & King 2006). In addition, F555W observations during the second epoch were included to allow the combination of proper motion information in the CMD. In particular, each observation epoch included two short exposures of ~50 s of integration time

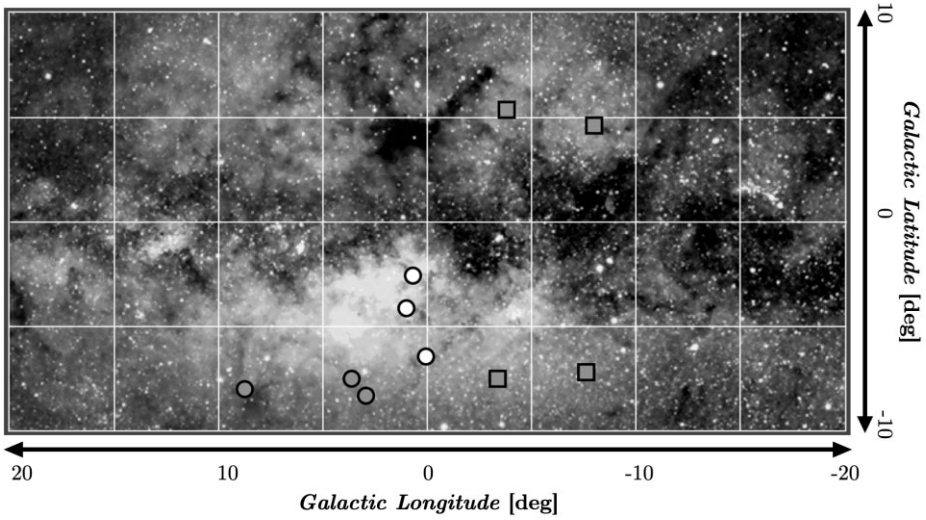

Figure 1. Fields in the Galactic bulge observed for this project, superimposed on an optical map (Mellinger 2009), from longitude $+20^\circ$ to -20°, and latitude -10° to $+10^\circ$. The fields presented on this work correspond to the grey squares while the data sets along the Galactic minor-axis (white circles) and near-side of the bar (grey circles) have been presented in Soto et al. (2012) and Soto et al. (2014), respectively.

Table 1. Summary of observations.

Field	Epoch	Exp.(s)	Filter	α, δ (J2000)	l,b	A_V
Field-4 + 5	2003 July 3	50(×2), 347(×4)	F814W	17 16 34, −29 34 27	356.°00, 4.°95	2.1
	2010 Jun 26	50(×2), 371(×4)	F814W			
	2010 Jun 26	50(×2), 416(×4)	F555W			
Field-8 + 5	2003 Jun 27	50(×2), 348(×4)	F814W	17 07 15, −33 02 43	352.°00, 4.°53	1.6
	2010 Jun 23	50(×2), 375(×4)	F814W			
	2010 Jun 23	50(×2), 420(×4)	F555W			
Field-4-7	2003 Aug 21	50(×2), 353(×4)	F814W	18 05 06, −35 54 10	356.°02,−7.°04	0.7
	2010 Aug 12	50(×2), 382(×4)	F814W			
	2010 Aug 12	50(×2), 427(×4)	F555W			
Field-8-7	2003 Jun 27	50(×2), 353(×4)	F814W	17 56 23, −38 56 13	352.°50,−7.°00	0.8
	2010 Jun 20	50(×2), 382(×4)	F814W			
	2010 Jun 20	50(×2), 427(×4)	F555W			

and four longer exposures of ∼350 s for the F814W and ∼ 420 s for the F555W observations taken for each field. These observations were dithered using a line pattern for the short exposures, while a box pattern was chosen for the four longer exposures.

A preliminary estimation of the accuracy of the proper motions was shown by KR02, where it was demonstrated how for a wide range of PSFs the centroid determination of stars with full width at half maximum (FWHM) and signal-to-noise ratio (S/N) is well-described by the expression $0.7 \times (FWHM) \times (S/N)^{-1}$. The latter equation, in the case of our ACS fields which typically have a PSF with $FWHM \simeq 0.09''$ and a star detected at 15σ, yields a precision of 4.2 mas. Thus, for a time baseline of 7 yr, such as our observations, we obtain a preliminary proper motion accuracy of ∼0.6 mas yr^{-1}, sufficient to map bulge kinematics.

3 PROPER MOTION MEASUREMENTS

The ACS/WFC has been on board the HST since 2002. One of the effects of the harsh radiation conditions in which the camera works can be seen as vertical trails that decrease as they move away from bright objects (Ubeda & Anderson 2012, and references therein). This charge transfer efficiency (CTE) issues affect the determination of fluxes and centroids of stars and therefore all the quantities derived from them, and since they are a consequence of the continuous exposure of the detector to cosmic rays, have increased over time. The effect of CTE is particularly significant for exposures taken after the Servicing Mission 4, in May 2009, and is currently addressed directly in the *Calibration Pipeline of ACS* (CALACS). Consequently, in our observations, we have used the CTE corrected images from CALACS (images with $*\_flc$ extension), which were processed using a refined version of the Anderson & Bedin (2010) procedure. Briefly, the software models the trails of the CTE in the original $\_flt$ images and inverts the modelled trail to build a version of each star without the CTE effects.

Another important effect to consider for proper motions are the geometric distortions; these have been addressed by means of the solutions specially designed for ACS/WFC (Anderson & King 2006), which allow obtaining positions for stellar sources in a distortion-free frame with astrometric accuracies of ∼0.01 pixels. The precision achieved is intrinsically related to the spatial variation of the PSF in the image, which in turn produces photometric accuracies of the order of ∼0.01 mags (Bellini et al. 2014).

The procedure to measure our proper motions follows the Anderson & King (2006) approach and can be summarized as follows. (i) For each $*\_flc$ exposure of each epoch we calculate the photometry using the publicly available software `img2xym_WFC.09x10.F`,

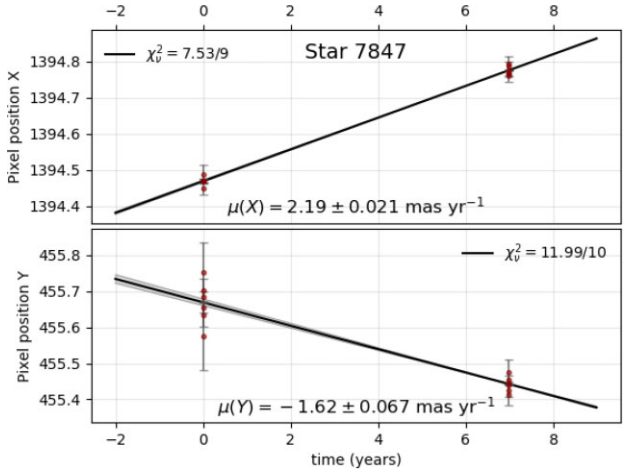

Figure 2. Example of the proper motion determinations in the master reference frame for a well-measured object in Field-4 + 5. The proper motion in each coordinate is estimated from an inverse variance-weighted straight-line fit to each positional time series, performed separately for the time series in X (top) and in Y (bottom). Shaded regions show the formal $\pm 1\sigma$ uncertainties in the predicted position. The best-fit proper motions and formal 1σ uncertainties are indicated as annotations (using a plate scale of 50.0 mas pix^{-1}), along with the reduced χ^2 values for the fits (the number of degrees of freedom being two less than the number of points surviving outlier-removal in each time-series). See Section 3 for details.

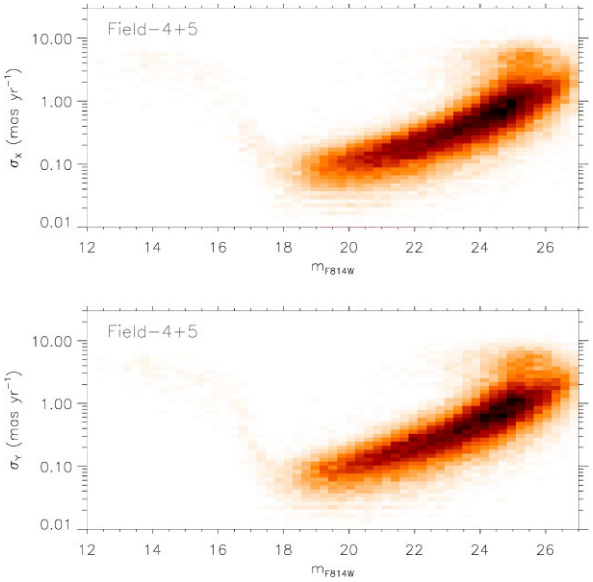

Figure 3. Uncertainties derived from the proper motion calculations in the X (top) and Y (bottom) direction for Field-4 + 5.

which, as previously mentioned, takes into account the ACS/WFC geometric distortions and filters used. (ii) A PSF library, provided by the software, is used to measure the stellar positions and fluxes. The PSFs are made of an array of 9 × 10 PSFs in each detector, where the PSF at each specific location corresponds to a bilinear interpolation of the nearest four PSFs in the grid. (iii) Armed with the photometry and positions for each exposure, we use the brightest unsaturated stars to align the individual exposures in a common frame and build a masterlist of stars we would identify in each exposure. The alignment of the images is improved by reducing in each step the uncertainty of the general six-parameter transformation that maps the masterlist into each individual exposure. We typically started out with a preliminary alignment by selecting for each epoch the brightest stars in one of the long exposures as a reference and limiting the selection to instrumental magnitudes $\lesssim -13$ and $\lesssim -11$ in long and short exposures, respectively. This preliminary alignment is later refined in a second iteration where the instrumental magnitudes of the selected stars discard saturated sources and is limited to stars $\simeq 2.5$ instrumental magnitudes below the bright limit imposed of -13.6 mag and -11.4 mag for long and short exposures, respectively. Subsequent iterations in the process further constrain the tolerance of the matches to a maximum of 0.04 pixels, where the number of stars used for the alignment has typically ranged from ∼3000 to ∼9000 stars depending on the crowding conditions on the respective field. (iv) The positions for each star in each image are then plotted in the master reference frame as a function of the observation date; the slope of the corresponding linear fit (see Fig. 2 for an example) is then the sought-after proper motion measurement for each star.

Fig. 3 shows the proper motion errors derived from the linear fit in Field-4 + 5. We can observe in Fig. 3 that a significant fraction of the stars $F814W < 22$ mag have errors in their positions <0.3 mas yr^{-1}; this value, just as a reference, for a distance of ∼ 10 kpc in a field in the far side at $l \sim -8°$, is translated in a velocity error ∼ 14 km s^{-1}. The latter value is significantly below the velocity dispersion of the bulge ∼ 100 km s^{-1} and therefore allows us to draw conclusions from the stellar kinematics observed safely.

It is important to mention that the proper motions derived are *relative*. We have arbitrarily assigned as zero the reference mean proper motion of the population of stars used to align the exposures. As we will see in Section 4.1, the transformation from *relative* to *absolute* will be thanks to the *Gaia* astrometric reference frame.

4 ANALYSIS

Fig. 4 and Table 2 show the proper motion distribution for our four fields. These distributions show, similarly to KR02, a longer tail towards positive μ_l, which we attribute to the foreground population, as explained below. Also, there is a suggestion in both fields at lower longitudes ($l \simeq 4$) of an opposite tilt with latitude in the contours of the distributions, which is also hinted in the Pearson correlation r_{lb} and velocity dispersion tensor σ^2_{lb}. Figs 5–8 show the respective binned CMDs colour-coded by including the proper motion information. The seminal work on this project, KR02, presented similar binned CMDs for fields along the minor axis: Baade's Window [(l,b)=1.13°,-3.77°)] and Sagittarius-I [(l,b) = 1.25°,-2.65°)], which showed a number of kinematic features that we can also observe in our fields:

(i) The first is the evident drift of the transverse proper motion μ_l for main sequence stars from a foreground population rotating in front of the bulge (stars with positive velocities) towards stellar populations which rotate at the far side of the bulge/bar (negative velocities). This effect is a clear indication that our observations penetrate through the bulge rotation.

(ii) The latter effect is also consistent with the observed dispersions, which for a given colour in the main sequence show a decrease in the dispersion towards fainter stars. This is in agreement with a distance effect, where stars located at greater distances and with consistent kinematics between them will have a smaller proper motion dispersion.

(iii) We also observe the same suggestion of a kinematically homogeneous population already reported in other bulge fields, like those along the Galactic minor-axis in KR02 and Cl08, which is

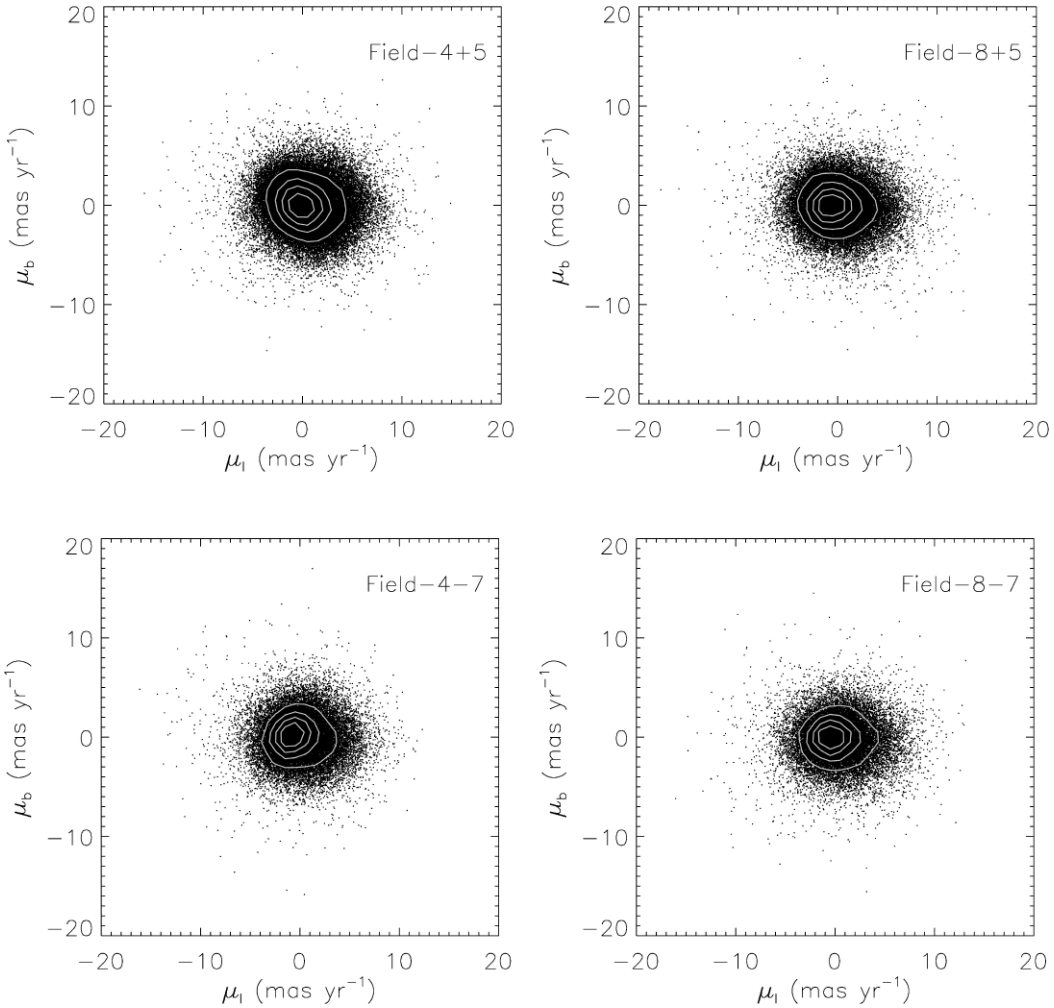

Figure 4. Proper motion distribution for the four fields presented in this work. Contours in each plot represent the 20 per cent, 40 per cent, 60 per cent, and 80 per cent of the maximum of the density distribution in the proper motions.

Table 2. Proper motion dispersions.

Field	N	σ_l (mas yr^{-1})	σ_b (mas yr^{-1})	σ^2_{lb} [a] (mas^2 yr^{-2})	r_{lb} [b]
Field-4 + 5	48 905	2.57 ± 0.01	2.25 ± 0.01	−0.717 ± 0.011	−0.103 ± 0.002
Field-8 + 5	31 213	2.58 ± 0.01	2.13 ± 0.01	−0.304 ± 0.010	−0.049 ± 0.002
Field-4-7	31 398	2.32 ± 0.01	2.01 ± 0.01	−0.004 ± 0.018	0.011 ± 0.003
Field-8-7	22 580	2.58 ± 0.01	2.14 ± 0.01	−0.083 ± 0.013	−0.007 ± 0.002

Notes.[a] Velocity ellipsoid tensor (Zhao et al. 1994): $\sigma^2_{ij} = \frac{N}{N-1}(\langle V_i V_j\rangle - \langle V_i\rangle\langle V_j\rangle)$.
[b] Pearson correlation coefficient.

consistent with a single isochrone and characteristic of an old stellar population.

In order to carefully study the effect of distances on our derived proper motions, we have carried out an analysis similar to that in KR02 and Cl08; the distance for each star is estimated based on its position in a CMD. Stars on the near side of the bulge will be moving differently with respect to us than those on the far side. Fig. 9 illustrates the procedure in which we have removed the CMD slope of a subsample of main sequence stars in Field-4 + 5, where we have reproduced the same procedure in the rest of our fields. In each case, we have traced a fiducial line to the highest concentration of stars in the main sequence, the photometric parallax estimate M^* is obtained by calculating the magnitude difference between each star of the selected section and its closest point to the fiducial line.

Fig. 10 shows the mean proper motions, in the subsample of main sequence stars, for the four fields on this work as a function of the photometric parallax M∗. Each bin corresponds to 500 stars for which we have calculated the velocity ellipsoid and iteratively rejected outliers beyond 3σ of the ellipsoid centre; error bars were obtained using a bootstrap Monte Carlo with 10 000 realizations. We observe similar behaviour in the four fields in spite of the differences in Galactic latitude and longitude, in particular, mean proper motion variations for different M∗ are significantly more pronounced in

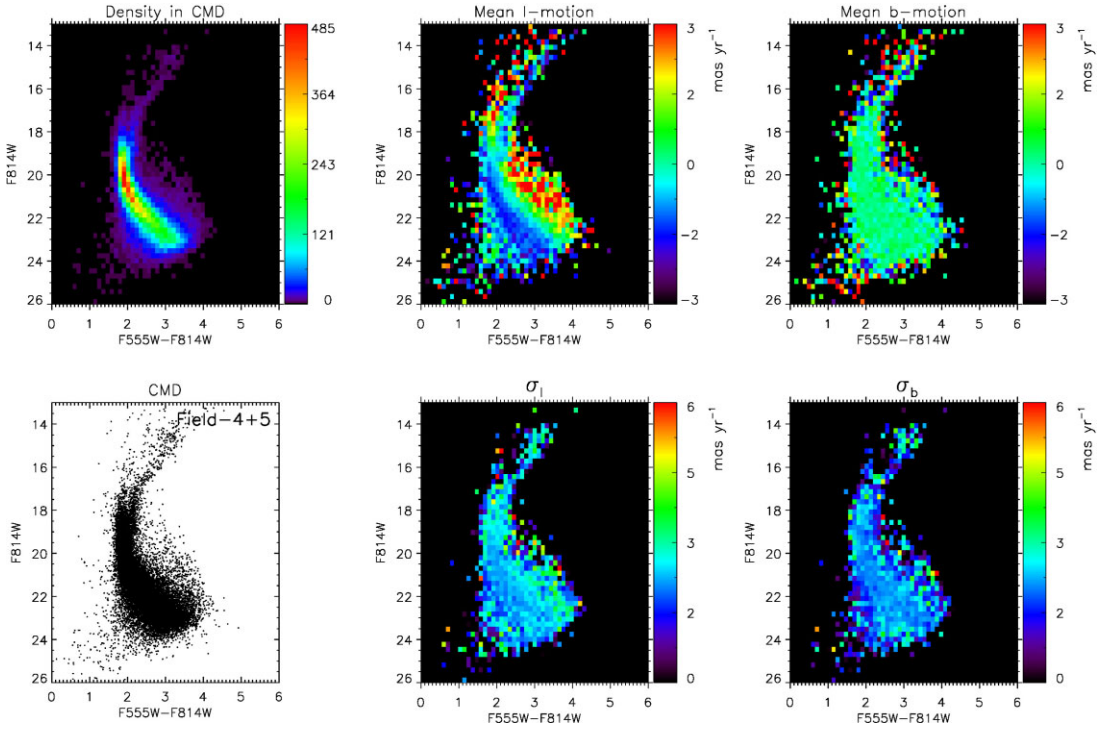

Figure 5. Binned CMDs of Field-4 + 5, with $n_{fit} \geq 8$. We have colour-coded each binned panel according to a different parameter. Top row, from left to right: stellar density, mean longitudinal proper motion, and mean latitudinal proper motion. Bottom row, from left to right: unbinned CMD, dispersion of the longitudinal proper motion, and dispersion of the latitudinal proper motions.

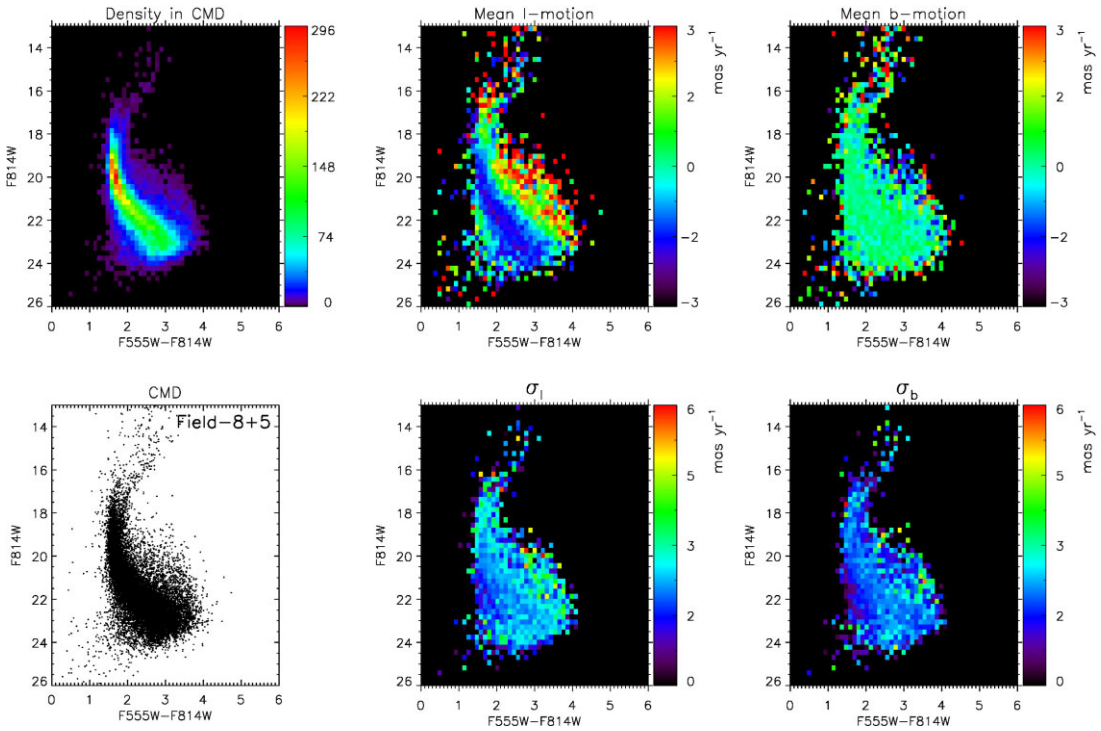

Figure 6. Same as Fig. 5, but for Field-8 + 5 with $n_{fit} \geq 8$.

the transverse direction than those in latitude. This is expected due to the effects of the Galactic rotation. Clarkson et al. (2018), in a careful study of the proper motion kinematics in the Sagittarius-I/SWEEPS field (l,b = 1.26°, −2.65°), included a classification of the metal-rich and metal-poor population based on the WFC3 Bulge Treasury Project (Brown et al. 2010); their analysis showed a higher amplitude rotation curve for the metal-rich sample in terms of the slope compared with the metal-poor for the mean μ_l. By comparison,

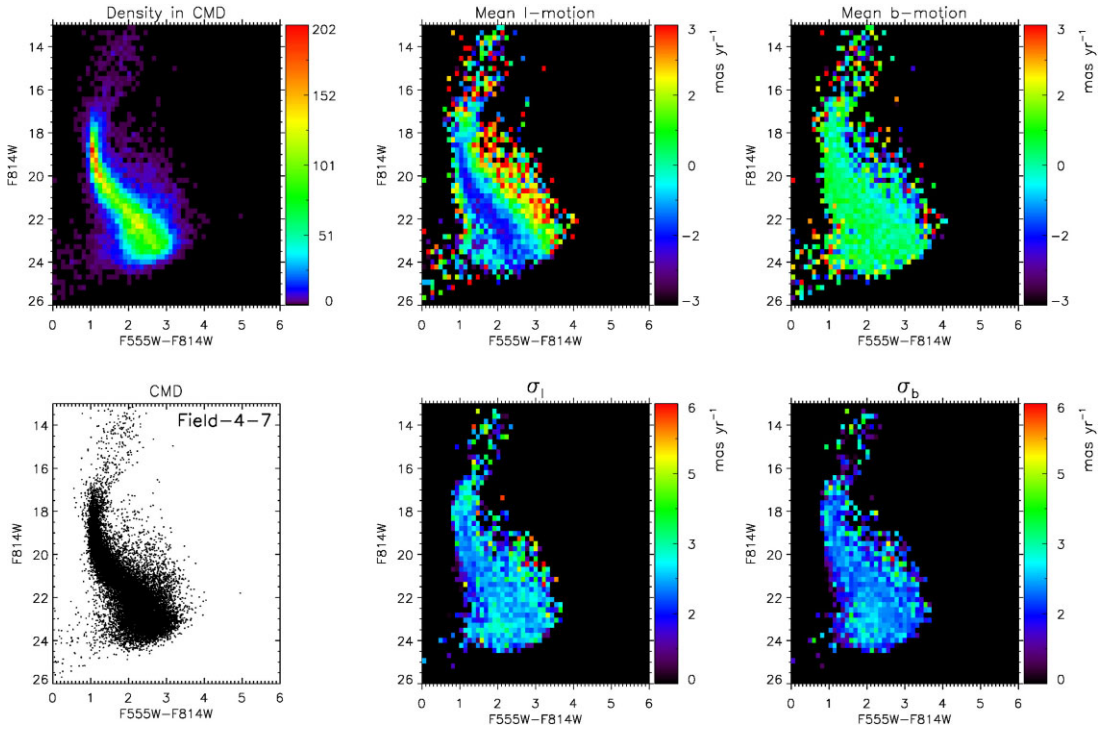

Figure 7. Same as Fig. 5, but for Field-4-7 with $n_{fit} \geq 8$.

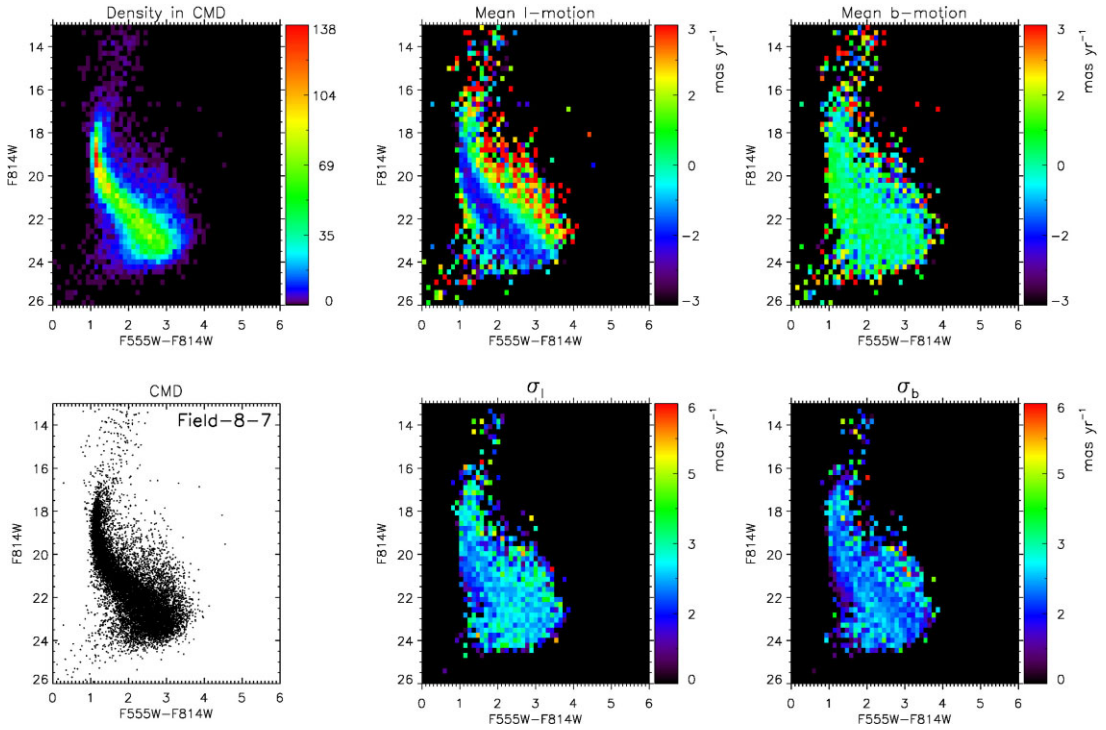

Figure 8. Same as Fig. 5, but for Field-8-7 with $n_{fit} \geq 8$.

our results show similar amplitude but lack the pronounced slope of the metal-rich sample. This result is also consistent with the mean μ_b observed by Clarkson et al. (2018), with a significantly smaller amplitude for the metal-poor and metal-rich subsamples, observed in all our fields. Another interesting feature observed in Fig. 10 is the increase in the mean transverse proper motion beyond the center of the Galaxy. This effect, which has already been observed in other bulge fields along the Galactic minor axis by KR02 and Cl08, appears in all our fields.

To compare the kinematics between the fields, we wish to convert photometric parallax estimates M^* into line of sight distances D^* that can also be compared between our fields. This conversion

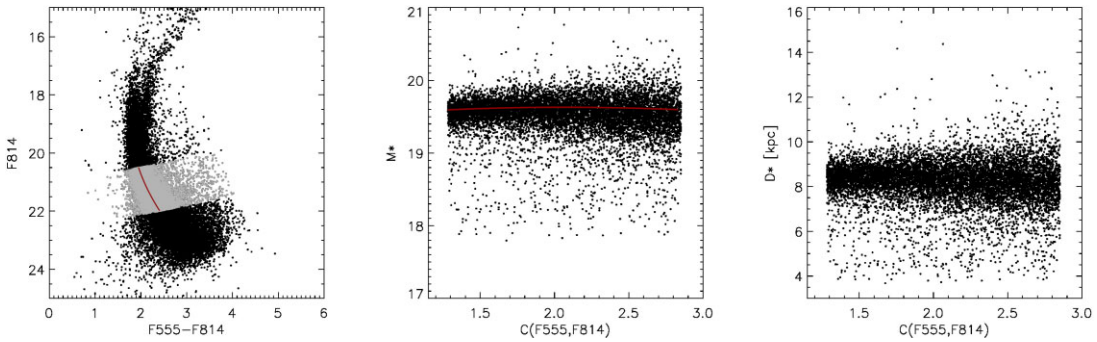

Figure 9. Selection of a subsample of the main sequence population, which has been used to calculate a photometric parallax M∗ and distances D∗ in Field-4 + 5. Left: CMD where a fiducial line (red solid) has been traced in the selected section (grey points) of the main sequence. Middle: photometric parallax M∗ as a function of the colour $C(F555, F814)$ of the selected subsample of main sequence stars. Right: distances of the main sequence subsample previously selected as a function of the colour $C(F555, F814)$, where the derived distances are with respect to the fiducial line.

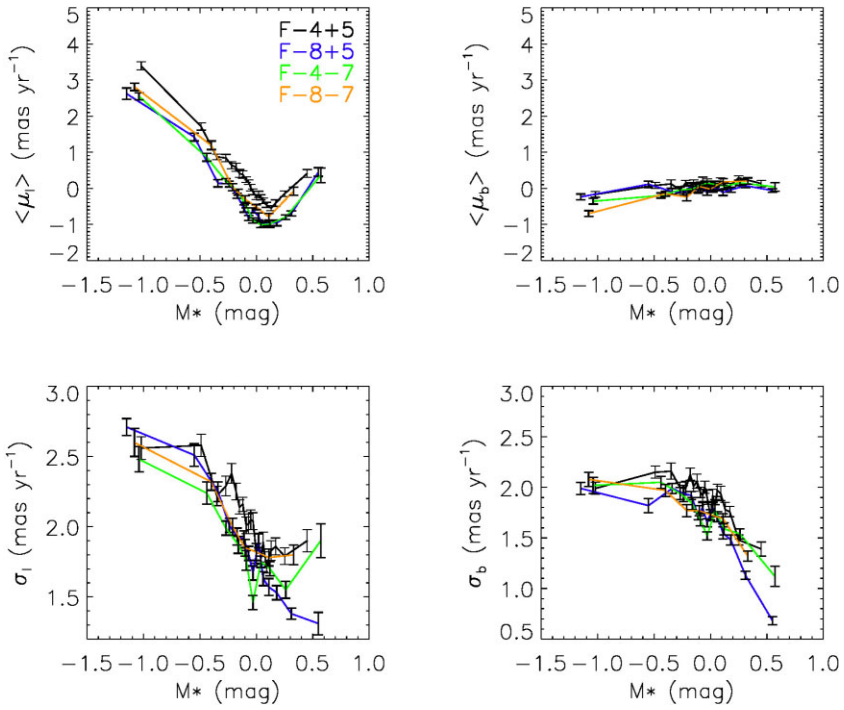

Figure 10. Mean proper motions and proper motion dispersions, as a function of the photometric parallax M∗, in the four fields presented on this work. Each point represents a bin of 500 stars for which we have calculated the velocity ellipsoid μ_l−μ_b, where we have rejected outliers beyond 3σ iteratively. Top left: mean proper motion μ_l as a function of M∗. Top right: mean proper motion μ_b as a function of M∗. Bottom row: same as top row, but for proper motion dispersions σ_l and σ_b.

is complicated by the intrinsic properties of the fields surveyed, including extinction, reddening, binary fraction, and particularly metallicity distributions, each of which can shift and broaden the M^* distributions by different amounts in each field. Indeed, inner bulge field areas near our target fields have been observed to show strong variations in metallicity distribution between fields at $|b| \approx 5^\circ$ and $|b| \approx 8^\circ$ (e.g. Zoccali et al. 2017). Star-by-star metallicity estimates are not yet available for our kinematic samples of interest. Rather than fold in assumptions and uncertainties about the intrinsic properties of the tracer populations, then, we instead assign distances to the fiducial populations with reference to a simple *geometric* model of the Galactic bulge/bar. Under this model, the line of sight distance to the fiducial population is estimated from the bar angle in the Galactic plane, ϕ_{bar}, and the position of the fields in Galactic coordinates (l, b), is given by

$$d_{\rm ref} = \frac{D_{\rm cen}}{\cos(b)\cos(l)\,(1 - \tan(l)\tan[\pi/2 - \phi_{\rm bar}])}. \quad (1)$$

We adopt a distance to the center of the Galaxy $D_{cen} = 8.3$ kpc (de Grijs & Bono 2016) and a bar inclination of $\phi_{bar} \simeq 27^\circ$ (e.g. Wegg & Gerhard 2013); this angle is compatible with recent values in the literature, as: $\sim 20^\circ$ from Simion et al. (2017); 28° from Clarke et al. (2019); $19.5 \pm 2.5^\circ$ from *Gaia* DR3 (Gaia Collaboration et al. 2023); and $29 \pm 3^\circ$ from Simion et al. (2021). In addition, we have also included the distances derived from the best geometric model by Simion et al. (2017). This work, based on dereddened VVV RC stars, indicates as a best-fitting model a boxy bulge with axial ratio (1:0.44:0.31). We remind the reader that our relative distances—and

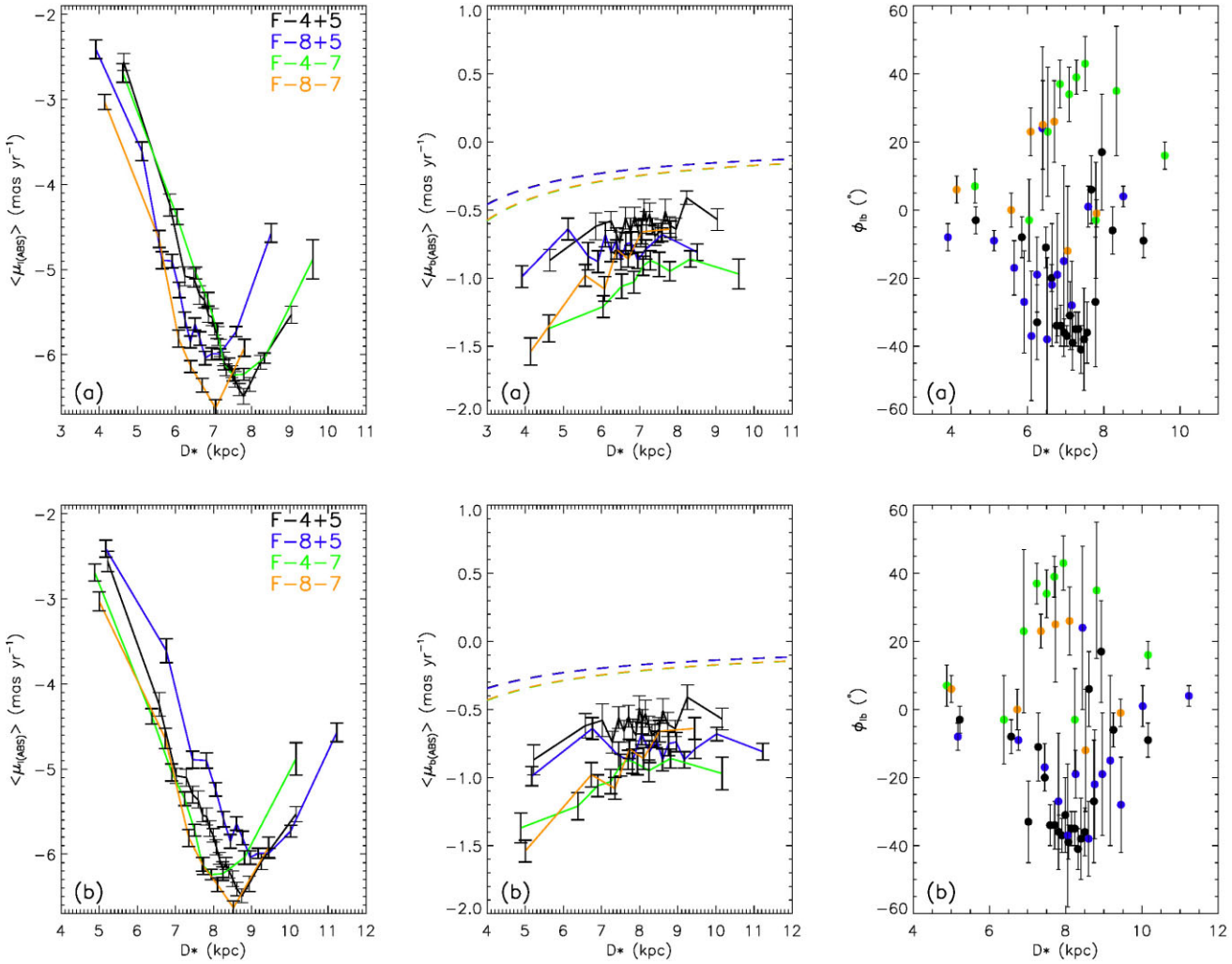

Figure 11. Top row (a): mean absolute proper motions μ_l (left) and μ_b (middle) transformed from relative using *Gaia* DR3 as the astrometric reference frame. Right: orientation angle ϕ_{lb} of the velocity ellipsoid in the l-b velocity plane. Distances $D*$ have been computed by transforming the photometric parallax $M*$ using the distance to the fields based on equation (1). Bottom row (b): same as top row, but for distances $D*$ to the fields derived from the best geometric model by Simion et al. (2017). Dashed lines in the middle panels represent the reflex Solar motion for each field according to the equations in Mignard (2000) and the peculiar solar motion determination by Ding et al. (2019).

thus conversions from proper motion to transverse velocity—depend on our model parameters for the bar spatial distribution.

4.1 Using *Gaia* DR3 to transform to absolute proper motions

The proper motions we have shown so far are relative. However, it is possible to use the *Gaia* absolute reference frame of its DR3 to transform our proper motions to absolute by cross-referencing stars in our catalogue that are also present in *Gaia*. We have performed such transformation for each one of our fields. The procedure is as follows, in each field we have downloaded and selected stars in the *Gaia* DR3 with reliable astrometry, that is, we use a similar criterion to Sanders et al. (2019) by selecting sources in *Gaia* with *astrometric_gof_al*<3 and *astrometric_excess_noise_sig*<2 and a maximum search radius of 1 arcsec. This selection allowed us to find for each of our fields 4233, 3598, 3420, and 2715 common stars in both catalogues for Field-4+5, Field-8 + 5, Field-4-7, and Field-8-7, respectively. The resultant cross-referenced sample HST-*Gaia* is then used to calculate the average offset by iteratively clipping outliers with a difference in position beyond 3σ, and adding that offset between the relative and absolute proper motions to the complete sample of HST proper motions. The result of the procedure can be seen in Fig. 11, which also includes the velocity ellipsoid angle ϕ_{lb} for each of the bins in each field. As expected, we observe a displacement of the mean proper motions curves with the new distances as a function of their Galactic positions. Thus, Fig. 11 shows a similar minimum in $\langle\mu_{l(ABS)}\rangle$ for fields with similar longitudes. At the same time, $\langle\mu_{b(ABS)}\rangle$ shows a separation for fields at negative and positive latitudes. In the latter, we have included the reflex solar motion as stated in Mignard (2000), using the peculiar solar motion ($u_\odot$, $v_\odot$, and $w_\odot$) determined by Ding, Zhu & Liu (2019) using *Gaia* DR2 main sequence stars. We can see that part of the distance trend observed for the $\langle\mu_{b(ABS)}\rangle$ can be explained by solar motion. However, there is still a significant offset that needs to be explained by the orbit distribution of the stellar population observed in the fields. Another interesting feature observed in Fig. 11, can be found in ϕ_{lb}, which despite the errorbars, shows some symmetry in Galactic latitude, with Field-4+5 and Field-8 + 5 exhibiting a minimum around ∼8–9 kpc of $D*$, while a maximum is found in Field-4-7 and Field-8-7. We note that this change in orientation of ϕ_{lb} is consistent with the shift of ϕ_{lb} with

distance observed in Soto et al. (2014), where the near-side bar field at the location (l, b) ∼(4,-7) had a $\phi_{lb} \simeq -25°$. We also noted in this calibration how the typical accuracy of the *Gaia* DR3 proper motions in the cross-referenced list increases over 2 mas yr^{-1} for F814W ≥ 19 mag, which limits the *Gaia* proper motion use in bulge kinematics to turn-off and RGB populations. This selection bias can also be observed in recent studies based on Gaia that include abundances and distances, such as those by Queiroz et al. (2021) or Rix et al. (2022). In particular, the cross-referenced catalog derived from the latter and our four fields contains just three bright (G < 14.17 mag) common stars in the whole sample, while the former has no matches. All this merely emphasizes the pertinence of the current work. Whether the characteristics previously described in the mean proper motions and others indicate intrinsic variation with location, or are instead entirely attributable to projection effects, requires a proper model of the dynamics of the different stellar components.

5 CONCLUSIONS AND FUTURE WORK

We have reported ∼100 000 new HST ACS/WFC stellar proper motions in four low foreground extinction fields on the far side of the Galactic bar/bulge at negative longitudes. Our proper motion results show stars with kinematics consistent with other bulge fields in the literature along the Galactic minor axis and the near-side of the bulge.

The increased number of stars in the fields presented here, compared to those on the bulge near-side, allows us to carefully observe the effect of the distance in the proper motion dispersions, a change in the orientation of the velocity ellipsoids in the (l, b) plane, and a significant bulge rotation, even in the fields as far as $l \simeq -8°$, from the Galactic minor-axis. All the effects described suggest a kinematically homogeneous sample, characteristic of an old stellar population. These and other features found in the derived proper motions pose an interesting opportunity for spectroscopic surveys capable of exploring MS stars in this magnitude range. This would allow connecting with the kinematics of other bulge populations better characterized, such as RC and RGB. In addition, effective constraints to dynamical models of the Milky Way can be obtained from our results, which is the next step of this project.

ACKNOWLEDGEMENTS

We would like to thank the anonymous referee for comments and advice that have greatly improved the clarity of the paper. LB and MVA acknowledge partial support by Consejo de Investigaciones Científicas y Técnicas (CONICET) and Secretaría de Ciencia y Técnica de la Universidad Nacional de Córdoba (SECyT). JLNC is grateful for the financial support received from the Southern Office of Aerospace Research and Development of the Air Force Office of the Scientific Research International Office of the United States (SOARD/AFOSR) through grants FA9550-18-1-0018 and FA9550-22-1-0037. JGF-T gratefully acknowledges the grant support provided by Proyecto Fondecyt Iniciación, number 11220340, and also from ANID Concurso de Fomento a la Vinculación Internacional para Instituciones de Investigación Regionales (Modalidad corta duración) Proyecto, number FOVI210020, and from the Joint Committee ESO-Government of Chile 2021 (ORP 023/2021), and from Becas Santander Movilidad Internacional Profesores 2022, Banco Santander Chile. AMK acknowledges support from grant AST-2009836 from the National Science Foundation. This work has made use of data from the European Space Agency (ESA) mission *Gaia* (https://www.cosmos.esa.int/gaia), processed by the *Gaia* Data Processing and Analysis Consortium (DPAC, https://www.cosmos.esa.int/web/gaia/dpac/consortium). Funding for the DPAC has been provided by national institutions, in particular the institutions participating in the *Gaia* Multilateral Agreement.

Based on observations made with the NASA/ESA Hubble Space Telescope, obtained from the data archive at the Space Telescope Institute. STScI is operated by the association of Universities for Research in Astronomy, Inc. under the NASA contract NAS 5-26555.

DATA AVAILABILITY

The data underlying this article will be shared on reasonable request to the corresponding author.

REFERENCES

Anderson J., Bedin L. R., 2010, PASP, 122, 1035
Anderson J., King I. R., 2006, Technical Report, PSFs, Photometry, and Astronomy for the ACS/WFC. Space Telescope Science Institute, Baltimore, MD
Babusiaux C. et al., 2010, A&A, 519, A77
Bellini A. et al., 2014, ApJ, 797, 115
Blitz L., Spergel D. N., 1991, ApJ, 379, 631
Brown T. M. et al., 2010, ApJ, 725, L19
Catchpole R. M., Whitelock P. A., Feast M. W., Hughes S. M. G., Irwin M., Alard C., 2016, MNRAS, 455, 2216
Clarke J. P., Wegg C., Gerhard O., Smith L. C., Lucas P. W., Wylie S. M., 2019, MNRAS, 489, 3519
Clarkson W. et al., 2008, ApJ, 684, 1110
Clarkson W. I. et al., 2018, ApJ, 858, 46
Cohen J. G. et al., 2010, ApJ, 711, L48
de Grijs R., Bono G., 2016, ApJS, 227, 5
de Vaucouleurs G., 1964, in Kerr F. J., ed., IAU Symp. Vol. 20, The Galaxy and the Magellanic Clouds. Australian Academy of Sciences, Canberra, p. 195
Debattista V. P., Gonzalez O. A., Sand erson R. E., El-Badry K., Garrison-Kimmel S., Wetzel A., Faucher-Giguère C.-A., Hopkins P. F., 2019, MNRAS, 485, 5073
Debattista V. P., Ness M., Gonzalez O. A., Freeman K., Zoccali M., Minniti D., 2017, MNRAS, 469, 1587
Ding P.-J., Zhu Z., Liu J.-C., 2019, Res. A&A, 19, 068
Dwek E. et al., 1995, ApJ, 445, 716
Epchtein N. et al., 1994, Ap&SS, 217, 3
Fernández-Trincado J. G., Beers T. C., Minniti D., Tang B., Villanova S., Geisler D., Pérez-Villegas A., Vieira K., 2020, A&A, 643, L4
Gaia Collaboration et al., 2016, A&A, 595, A1
Gaia Collaboration et al., 2018a, A&A, 616, A11
Gaia Collaboration et al., 2018b, A&A, 616, A12
Gaia Collaboration et al., 2023, A&A, 674, A37
Gaia Collaboration et al., 2023, A&A, 674, A1
Gennaro M., Tchernyshyov K., Brown T. M., Gordon K. D., 2015, ApJ, 808, 45
Hasselquist S. et al., 2020, ApJ, 901, 109
Johnson C. I., Rich R. M., Kobayashi C., Kunder A., Koch A., 2014, AJ, 148, 67
Kuijken K., 2004, in Clemens D., Shah R., Brainerd T.eds, ASP Conf. Ser. Vol. 317, Milky Way Surveys: The Structure and Evolution of our Galaxy, Astron. Soc. Pac., San Francisco, p. 310
Kuijken K., Rich R. M., 2002, AJ, 124, 2054
Lian J. et al., 2021, MNRAS, 500, 282
McWilliam A., Rich R. M., 1994, ApJS, 91, 749
Mellinger A., 2009, PASP 121 1180
Mignard F., 2000, A&A, 354, 522
Minniti D. et al., 2010, New A, 15, 433
Nataf D. M., Udalski A., Gould A., Fouqué P., Stanek K. Z., 2010, ApJ, 721, L28

Ness M. et al., 2013, MNRAS, 430, 836
Ortolani S., Renzini A., Gilmozzi R., Marconi G., Barbuy B., Bica E., Rich R. M., 1995, Nature, 377, 701
Queiroz A. B. A. et al., 2021, A&A, 656, A156
Recio-Blanco A. et al., 2017, A&A, 602, L14
Rix H.-W. et al., 2022, ApJ, 941, 45
Robin A. C., Marshall D. J., Schultheis M., Reylé C., 2012, A&A, 538, A106
Rojas-Arriagada A. et al., 2020, MNRAS, 499, 1037
Sanders J. L., Smith L., Evans N. W., Lucas P., 2019, MNRAS, 487, 5188
Savino A., Koch A., Prudil Z., Kunder A., Smolec R., 2020, A&A, 641, A96
Shen J., Rich R. M., Kormendy J., Howard C. D., De Propris R., Kunder A., 2010, ApJ, 720, L72
Simion I. T., Belokurov V., Irwin M., Koposov S. E., Gonzalez-Fernandez C., Robin A. C., Shen J., Li Z. Y., 2017, MNRAS, 471, 4323
Simion I. T., Shen J., Koposov S. E., Ness M., Freeman K., Bland-Hawthorn J., Lewis G. F., 2021, MNRAS, 502, 1740
Skrutskie M. F. et al., 2006, AJ, 131, 1163
Soto M., Kuijken K., Rich R. M., 2012, A&A, 540, A48
Soto M., Rich R. M., Kuijken K., 2007, ApJ, 665, L31
Soto M., Zeballos H., Kuijken K., Rich R. M., Kunder A., Astraatmadja T., 2014, A&A, 562, A41
Spaenhauer A., Jones B. F., Whitford A. E., 1992, AJ, 103, 297
Ubeda L., Anderson J., 2012, Technical Report, Study of the Evolution of the ACS/WFC Charge Transfer Efficiency. Space Telescope Science Institute, Baltimore, MD
Valenti E., Zoccali M., Renzini A., Brown T. M., Gonzalez O. A., Minniti D., Debattista V. P., Mayer L., 2013, A&A, 559, A98
Vanhollebeke E., Groenewegen M. A. T., Girardi L., 2009, A&A, 498, 95
Vieira K. et al., 2007, AJ, 134, 1432
Wegg C., Gerhard O., 2013, MNRAS, 435, 1874
Weiland J. L. et al., 1994, ApJ, 425, L81
Zasowski G. et al., 2019, ApJ, 870, 138
Zhao H., Spergel D. N., Rich R. M., 1994, AJ, 108, 2154
Zoccali M. et al., 2017, A&A, 599, A12
Zoccali M., Valenti E., 2016, PASA, 33, e025

This paper has been typeset from a TEX/LATEX file prepared by the author.